CO_2-driven diffusiophoresis for maintaining a bacteria-free surface

Suin Shim[1,*], Sepideh Khodaparast[2], Ching-Yao Lai[3], Jing Yan[4], Jesse T. Ault[5], Bhargav Rallabandi[6], Orest Shardt[7], and Howard A. Stone[1,†]

[1]*Department of Mechanical and Aerospace Engineering, Princeton University, Princeton, NJ 08544, USA*

[2]*School of Mechanical Engineering, University of Leeds, Leeds LS2 9JT, UK*

[3]*Lamont-Doherty Earth Observatory, Columbia University, Palisades, NY 10964, USA*

[4]*Department of Molecular, Cellular and Developmental Biology, Quantitative Biology Institute, Yale University, C144 Yale Science Building, New Haven, CT, 06511, USA*

[5]*School of Engineering, Brown University, Providence, Rhode Island 02912, USA*

[6]*Department of Mechanical Engineering, University of California, Riverside, California 92521, USA*

[7]*Bernal Institute and School of Engineering, University of Limerick, Castletroy, Limerick, V94 T9PX, Ireland*

(Dated: January 05. 2021)

In the Supplementary Information (SI), we present system details, model calculations for particle distributions driven by CO_2 diffusiophoresis, and supplementary experiments.

List of supplementary videos

V1: Charged particles near a dissolving CO_2 bubble (HS-B)
V2: Macroscopic particle accumulation and exclusion near a CO_2 bubble (HS-B)
V3: Macroscopic particle accumulation and exclusion near a fixed CO_2 source (HS-PC)
V4: Diffusiophoresis of *V. cholerae* cells near a fixed CO_2 source (HS-PC)
V5: Diffusiophoretic motion of *P. aeruginosa* cells near a fixed CO_2 source (HS-PC)

* sshim@princeton.edu
† hastone@princeton.edu

I. System description and model calculations

We set up a one-dimensional model to understand particle distribution relative to the bubble interface and the PDMS boundary. Prior to setting up the model, we describe the detailed geometry used in the experiments, and define nondimensional variables frequently mentioned in the main text.

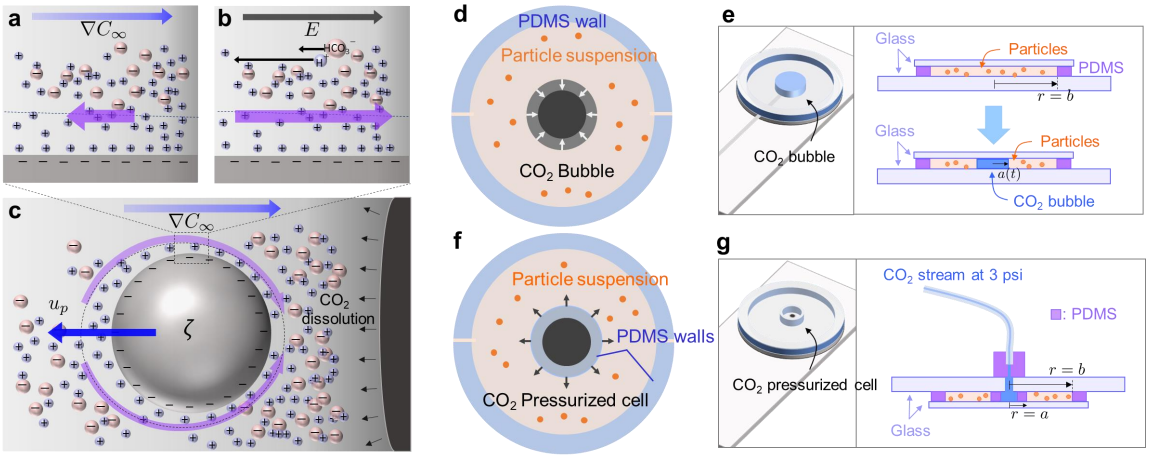

Figure S1: CO_2-driven diffusiophoresis in Hele-Shaw cells. (a-c) Schematic of particle (negatively charged) motion near a CO_2 source. (a) Chemiphoretic and (b) electrophoretic contributions to the diffusiophoretic motion are in opposite directions with electrophoresis dominating, (c) a negatively charged particle migrates away from the CO_2 source. (d-e) Schematics of CO_2 bubble experiments. A CO_2 bubble of initial radius a_0 is injected into a Hele-Shaw cell that is initially filled with a particle suspension. (f-g) Schematics of fixed boundary experiments. In the Hele-Shaw cell, we put one more circular spacer (PDMS) to have an inner cell (radius a) in which CO_2 can be pressurized. The pressurized CO_2 then dissolves into the particle suspension through the gas permeable PDMS wall. Radius of the outer PDMS wall is $b = 11$ mm. The height of the Hele-Shaw cell is 500 μm.

CO_2-driven diffusiophoresis in an aqueous phase is achieved by dissolution and dissociation of CO_2 in water, which is described approximately by

$$CO_2 + H_2O \underset{k_r}{\overset{k_f}{\rightleftharpoons}} H^+ + HCO_3^- \ . \tag{1}$$

Due to the large difference in the diffusivity of the two ions, $D_{H^+} = 9.31\times10^{-9}$ m^{2}s^{-1} and $D_{HCO_3^-} = 1.19\times10^{-9}$ m^{2}s^{-1}, a large diffusion potential $\phi_2 - \phi_1 = -\dfrac{kT}{e}\dfrac{D_+ - D_-}{D_+ + D_-}\ln\dfrac{c_2}{c_1} \approx -60$ mV (for $c_2/c_1 = 20$; $c_1 = 2.7\times10^{-6}$ M and $c_2 = 5.37\times10^{-5}$ M, concentrations of ions in equilibrium with ≈ 20 kPa and ≈ 0.05 kPa CO_2)[2] is created and diffusiophoresis of charged particles is achieved with a dominant electrophoretic contribution (Fig. S1(b,c)). The diffusiophoretic velocity u_p of particles under the ion concentration gradient ∇c_i is written as $u_p = \Gamma_p \nabla \ln c_i$, where Γ_p is the diffusiophoretic mobility of the particles under concentration gradient of a z:z electrolyte;[4]

$$\Gamma_p = \frac{\epsilon}{\mu}\frac{kT}{ze}\left[\beta\zeta - \frac{2kT}{ze}\ln\left(1 - \tanh^2\frac{ze\zeta}{4kT}\right)\right] \ . \tag{2}$$

The formula for the mobility is derived by assuming a thin double layer and local charge neutrality. Here ϵ, μ, k, T, e and ζ are, respectively, dielectric permittivity of the solution, dynamic viscosity of the solution, Boltzmann constant, absolute temperature and the zeta potential of the particle. $\beta = \dfrac{D_+ - D_-}{D_+ + D_-}$ is the diffusivity difference factor, which determines the strength of the local electric field $\mathbf{E} = -\nabla\phi$ induced by the difference in diffusivities of the ions. In Fig. S1(a-c), the direction of diffusiophoresis of negatively charged particle is described schematically. As the electrophoresis and the chemiphoresis contributions to the diffusiophoretic motion are in opposite directions, with the dominant contribution due to electrophoresis, a negatively charged particle is expected to migrate away from the source of CO_2, following the rapidly diffusing H^+ ions.

We study CO_2-driven diffusiophoresis in two different systems; one with a moving boundary and the other with a fixed boundary (Fig. S1(d-g)). In the first system, where a CO_2 bubble (initial radius $a_0 \approx 2.5$-3 mm) is introduced in a circular Hele-Shaw cell (Fig. S1(d,e)), we observe a distribution of charged particles near the shrinking bubble interface, which moves radially inward as CO_2 dissolves into the solution. In the second experimental system (Fig. 1(f,g)), CO_2 is pressurized at a constant pressure (3 psig) in an inner cell (radius $a = 3$ mm) that is concentrically located with the outer wall of Hele-Shaw cell. As a result, we observe and track the particles near the fixed boundary where CO_2 dissolves through a PDMS wall into a particle suspension.

In the bubble dissolution system, a CO_2 bubble with initial radius a_0 shrinks at a typical speed $\frac{da}{dt} \approx \frac{D_1}{a_0} \approx O(0.1\text{-}1)$ μm/s until the gas exchange reaches steady state within $\approx \tau = t/a_0^2/D_1 = 1$.[1] D_1 is the diffusivity of CO_2 in water. The typical diffusiophoretic velocity u_p scales as $u_p \approx \frac{\Gamma_p}{a_0} \approx O(0.1\text{-}1)$ μm/s. The relative motion of particles and the shrinking interface creates charge dependent particle distribution near the equilibrium bubble.

In both systems, we observe local and macroscopic particle accumulation or exclusion. With one-dimensional model, we will calculate particle distribution along the radius of Hele-Shaw cell, and compare the macroscopic boundaries of particle accumulation and exclusion with the experimental measurements. The local exclusion zone (EZ) growth in the fixed boundary system (HS-BC) is shown in Fig. S2, and the growth of EZ is proportional to $\sqrt{t}$ at early times (Fig. S2(c)). The boundary of EZ in the experiments is defined as the radial position where the normalized intensity value is 1.

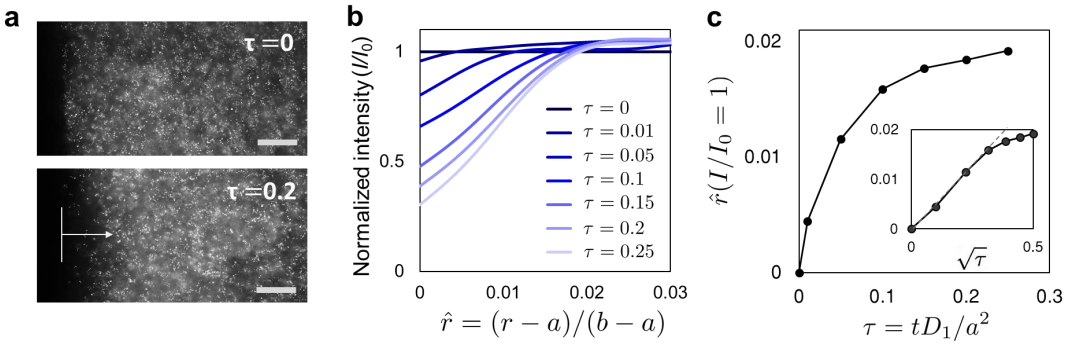

Figure S2: Growth of local exclusion zone (EZ) in HS-PC system. (a) Images showing exclusion of polystyrene particles near the PDMS wall. Scale bars are 100 μm. (b) Normalized intensity plotted versus radial position. We define the boundary of the local exclusion zone as the radial position where the normalized intensity is 1. (c) Growth of EZ plotted versus time. Inset: Growth of EZ plotted versus $\sqrt{\tau}$ showing early dependence on $\sqrt{t}$.

A. Diffusiophoresis of particles near a dissolving CO_2 bubble

Consider a CO_2 bubble generated in a Hele-Shaw cell (Fig. S3(a)), dissolving into the aqueous suspension of particles. We start by writing one dimensional diffusion-reaction equations for CO_2 ions and air. Let $c_m(r,t)$ $(m = 1, 2)$ be the mass concentration of CO_2 and air, and $c_i(r,t)$ be the concentration of ions. Then for CO_2, ions and air, we can write

$$\frac{\partial c_1}{\partial t} + \frac{a}{r}\frac{da}{dt}\frac{\partial c_1}{\partial r} = \frac{D_1}{r}\frac{\partial}{\partial r}\left(r\frac{\partial c_1}{\partial r}\right) - (k_f c_1 - k_r c_i^2) \tag{3}$$

$$\frac{\partial c_i}{\partial t} + \frac{a}{r}\frac{da}{dt}\frac{\partial c_i}{\partial r} = \frac{D_A}{r}\frac{\partial}{\partial r}\left(r\frac{\partial c_i}{\partial r}\right) + (k_f c_1 - k_r c_i^2) \tag{4}$$

$$\frac{\partial c_2}{\partial t} + \frac{a}{r}\frac{da}{dt}\frac{\partial c_2}{\partial r} = \frac{D_2}{r}\frac{\partial}{\partial r}\left(r\frac{\partial c_2}{\partial r}\right) \ , \tag{5}$$

where $a(t)$, D_1, D_A and D_2 are, respectively, the radius of the bubble, CO_2, ambipolar and air diffusivities. Before solving the equations with appropriate boundary conditions, we would like to evaluate the influence of

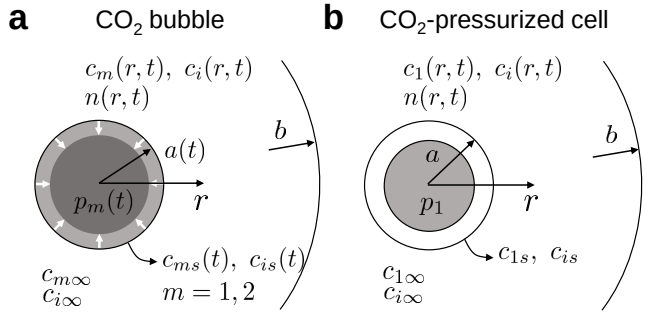

Figure S3: Schematics for model calculations: (a) CO_2-driven diffusiophoresis near a dissolving bubble, and (b) near a CO_2-pressurized cell.

the reaction kinetics on the bubble dynamics by rescaling the equations (3) and (4). Let

$$\bar{c}_1 = \frac{c_1}{c_{1s}(0)} \ , \quad \bar{c}_i = \frac{c_i}{c_{is}(0)} \ , \quad R = \frac{a}{a_0} \ , \quad \bar{r} = \frac{r}{a_0} \ , \quad \tau = \frac{t}{a_0^2/D_1} \ , \tag{6}$$

where $c_{1s}(0)$ and $c_{is}(0)$ are concentrations of CO_2 and ions at the bubble interface at $t = 0$. Then

$$(3) \Rightarrow \frac{\partial \bar{c}_1}{\partial \tau} + \frac{R}{\bar{r}} \frac{dR}{d\tau} \frac{\partial \bar{c}_1}{\partial \bar{r}} = \frac{\partial^2 \bar{c}_1}{\partial \bar{r}^2} + \frac{1}{\bar{r}} \frac{\partial \bar{c}_1}{\partial \bar{r}} - \frac{\tau_D}{\tau_i} \left(\frac{k_f}{k_r c_{1s}} \right)^{\frac{1}{2}} (\bar{c}_1 - \bar{c}_i^2) \ , \tag{7}$$

where $\tau_D = \dfrac{a_0^2}{D_1}$, $\tau_i = (k_r c_{is})^{-1}$ and $\left(\dfrac{k_f}{k_r c_{1s}} \right)^{\frac{1}{2}} = \dfrac{c_{is}(0)}{c_{1s}(0)}$.

$$(4) \Rightarrow \frac{\tau_i}{\tau_D} \left[\frac{\partial \bar{c}_i}{\partial \tau} + \frac{R}{\bar{r}} \frac{dR}{d\tau} \frac{\partial \bar{c}_i}{\partial \bar{r}} - \bar{D}_A \left(\frac{\partial^2 \bar{c}_i}{\partial \bar{r}^2} + \frac{1}{\bar{r}} \frac{\partial \bar{c}_i}{\partial \bar{r}} \right) \right] = \bar{c}_1 - \bar{c}_i^2 \ , \tag{8}$$

where $\bar{D}_A = \frac{D_A}{D_1}$.

Therefore, we obtain for $\tau_i \ll \tau_D$ and $\dfrac{c_{is}(0)}{c_{1s}(0)} \ll 1$,

$$\bar{c}_1 - \bar{c}_i^2 = 0 \ \text{ and } \ \frac{\partial \bar{c}_1}{\partial \tau} + \frac{R}{\bar{r}} \frac{dR}{d\tau} \frac{\partial \bar{c}_1}{\partial r} = \frac{\partial^2 \bar{c}_1}{\partial \bar{r}^2} + \frac{1}{\bar{r}} \frac{\partial \bar{c}_1}{\partial \bar{r}} \ . \tag{9}$$

In other words, we can decouple the reaction and dissolution of CO_2, given that the system parameter satisfies the conditions $\tau_i \ll \tau_D$ and $\dfrac{c_{is}(0)}{c_{1s}(0)} \ll 1$. As a result, we can assume local chemical equilibrium everywhere in the liquid phase, and the equation $k_f c_1 - k_r c_i^2 = 0$ holds. The ion concentration $c_i = \sqrt{k_f c_1 / k_r}$ can be obtained by knowing the concentration c_1 of dissolved CO_2. Now the CO_2 and ion concentrations are decoupled, CO_2 concentration can be solved by considering the multicomponent gas dissolution in the system.

Now let's consider the equations for multicomponent gas dissolution.

$$\frac{\partial c_m}{\partial t} + \frac{a}{r} \frac{da}{dt} \frac{\partial c_m}{\partial r} = \frac{D_m}{r} \frac{\partial}{\partial r} \left(r \frac{\partial c_m}{\partial r} \right) \ . \tag{10}$$

Mass conservation at the bubble can be written as

$$\begin{aligned} &\frac{d}{dt}(\pi a^2 h \rho_m) + 2\pi a h \left(\frac{a}{r} \frac{da}{dt} c_m \right)_{r=a} = 2\pi a h D_m \left(\frac{\partial c_m}{\partial r} \right)_{r=a} \\ \Rightarrow \quad &\rho_m \frac{da}{dt} + \frac{a}{2} \frac{d\rho_m}{dt} + c_{ms} \frac{da}{dt} = D_m \left(\frac{\partial c_m}{\partial r} \right)_{r=a} \ , \end{aligned} \tag{11}$$

where ρ_m is the density of gases ($m = 1, 2$) in the bubble. Applying ideal gas law $p_m = \rho_m R_{gm} T$, where p_m, R_{gm} and T are, respectively, the partial pressure of gases in the bubble, specific gas constants, and the absolute temperature,

$$\frac{1}{R_{gm}T}\left[(1 + k_m R_{gm} T) p_m \frac{da}{dt} + \frac{a}{2}\frac{dp_m}{dt}\right] = D_m \left(\frac{\partial c_m}{\partial r}\right)_{r=a} . \tag{12}$$

Note that the Henry's law $c_{ms} = k_m p_m$ is used with the Henry's law constant k_m ($m = 1, 2$). At the bubble interface,

$$p_1 + p_2 = p_a + \frac{\gamma}{a} , \quad \text{and} \quad \frac{dp_1}{dt} + \frac{dp_2}{dt} = -\frac{\gamma}{a^2}\frac{da}{dt} , \tag{13}$$

where γ is the interfacial tension.

Equation (12) can be written for each species as below.

$$\frac{1}{R_{g1}T}\left[(1 + A) p_1 \frac{da}{dt} + \frac{a}{2}\frac{dp_1}{dt}\right] = D_1 \left(\frac{\partial c_1}{\partial r}\right)_{r=a} \tag{14}$$

$$\frac{1}{R_{g2}T}\left[(1 + \alpha A B) p_2 \frac{da}{dt} + \frac{a}{2}\frac{dp_2}{dt}\right] = D_2 \left(\frac{\partial c_2}{\partial r}\right)_{r=a} , \tag{15}$$

where $\alpha = R_{g2}/R_{g1}$, $A = k_1 R_{g1} T$ and $B = k_2/k_1$. Summing up these two equations we obtain

$$\frac{da}{dt} = \frac{D_1 \left(\frac{\partial c_1}{\partial r}\right)_a + \alpha D_2 \left(\frac{\partial c_2}{\partial r}\right)_a}{\frac{1}{R_{g1}T}\left[p_a + \frac{\gamma}{2a} + A[p_1 + \alpha B p_2)\right]} . \tag{16}$$

The initial and boundary conditions for $c_m(r, t)$, $p_m(t)$ and $a(t)$ are ($m = 1, 2$),

$$c_m(r, 0) = c_{m\infty} \tag{17a}$$

$$c_m(a, t) = c_{ms}(t) \tag{17b}$$

$$\frac{\partial c_m}{\partial r}(b, t) = 0 \tag{17c}$$

$$p_1(0) = p_a + \frac{\gamma}{a_0} \tag{17d}$$

$$p_2(0) = 0 \tag{17e}$$

$$a(0) = a_0 \tag{17f}$$

where $c_{m\infty}$ is the concentration of gases in the liquid that is in equilibrium with atmospheric condition. Note that we assume the wall $r = b$ to be impermeable to gas. In the experiments, the wall is made of PDMS, which is permeable to CO_2. However the effect of wall $r = b$ is expected to become significant for times later than the typical time scale of experiments ($t > \tau_D = \frac{a_0^2}{D_1}$). Therefore, the boundary condition $\frac{\partial c_1}{\partial r}\big|_{r=b} = 0$ is reasonable.

By solving equations (10) and (14-16) with appropriate boundary conditions we obtain $c_1(r, t)$, and from the chemical equilibrium condition we obtain $c_i(r, t)$ which is used for calculations of diffusiophoretic velocity.

The diffusiophoretic velocity of particles in r-direction is

$$u_p = \Gamma_p \frac{\partial \ln c_i}{\partial r} . \tag{18}$$

Then the particle distribution in the liquid phase can be obtained by solving

$$\frac{\partial n}{\partial t} + \frac{1}{r}\frac{\partial}{\partial r}\left[r\left(u_p + \frac{a}{r}\frac{da}{dt}\right) n\right] = \frac{D_p}{r}\frac{\partial}{\partial r}\left(r\frac{\partial n}{\partial r}\right) , \tag{19}$$

where D_p is the diffusivity of particles. Note that in this model we do not consider the volume of a single particle and also particle-particle interactions. Boundary conditions for $n(r,t)$ are,

$$n(r,0) = n_0 \tag{20a}$$

$$\left.\frac{\partial n}{\partial r}\right|_{r=b} = 0 \ . \tag{20b}$$

The boundary condition at $r = a$ can be written separately for different surface charges of the particles. Since we expect the positively charged particles to accumulate at the moving interface, $\left.\frac{\partial n}{\partial r}\right|_{r=a} = 0$ for $\Gamma_p > 0$. Negatively charged particles always migrate away from the moving interface, which means that we can simply assume $n(a, t > 0) = 0$ for $\Gamma_p < 0$.

The equations can be nondimensionalized by defining

$$\bar{c}_1 = \frac{c_1}{c_{1s}(t)} \ , \ \bar{c}_2 = \frac{c_2 - c_{2\infty}}{c_{2s}(t) - c_{2\infty}} \ , \ \bar{c}_i = \frac{c_i}{c_{is}(t)} \ , \ \bar{n} = \frac{n}{n_0} \ , \ \bar{p}_1 = \frac{p_1}{p_a} \ , \ \bar{p}_2 = \frac{p_2}{p_a} \ , \ \Gamma = \frac{\gamma}{a_0 p_a} \ , \ \bar{D}_p = \frac{D_p}{D_1} \ ,$$
$$\bar{\Gamma}_p = \frac{\Gamma_p}{D_1} \ , \ Q = \frac{D_2}{D_1} \ , \ B = \frac{k_2}{k_1} \ , \ A = k_1 R_{g1} T \ , \ \tau = \frac{t}{a_0^2/D_1} \ , \ R = \frac{a}{a_0} \ , \ \bar{b} = \frac{b}{a_0} \ , \ \bar{r} = \frac{r}{a_0} \ . \tag{21}$$

Note that the definitions for $\bar{c}_m$ and $\bar{c}_i$, we now use $c_{ms}(t)$ and $c_{is}(t)$ for nondimensionalization. The nondimensional equations are,

$$\bar{c}_i = \sqrt{\bar{c}_1} \tag{22}$$

$$\frac{\partial \bar{c}_1}{\partial \tau} + \frac{\bar{c}_1}{\bar{p}_1}\frac{\partial \bar{p}_1}{\partial \tau} + \frac{R}{\bar{r}}\frac{dR}{d\tau}\frac{\partial \bar{c}_1}{\partial \bar{r}} = \frac{\partial^2 \bar{c}_1}{\partial \bar{r}^2} + \frac{1}{\bar{r}}\frac{\partial \bar{c}_1}{\partial \bar{r}} \tag{23}$$

$$\frac{\partial \bar{c}_2}{\partial \tau} + \frac{\bar{c}_2}{\bar{p} - 1}\frac{d\bar{p}_2}{d\tau} + \frac{R}{\bar{r}}\frac{dR}{d\tau}\frac{\partial \bar{c}_2}{\partial \bar{r}} = Q\left(\frac{\partial^2 \bar{c}_2}{\partial \bar{r}^2} + \frac{1}{\bar{r}}\frac{\partial \bar{c}_2}{\partial \bar{r}}\right) \tag{24}$$

$$\frac{dR}{d\tau} = \frac{\bar{p}_1\left(\frac{\partial \bar{c}_1}{\partial \bar{r}}\right)_R + \alpha Q B(\bar{p}_2 - 1)\left(\frac{\partial \bar{c}_2}{\partial \bar{r}}\right)_R}{\frac{1}{A}\left[1 + \frac{\Gamma}{2R}\right] + (\bar{p}_1 + \alpha B \bar{p}_2)} \tag{25}$$

$$\frac{1}{A}\left[(1 + A)\bar{p}_1\frac{dR}{d\tau} + \frac{R}{2}\frac{d\bar{p}_1}{d\tau}\right] = \bar{p}_1\left(\frac{\partial \bar{c}_1}{\partial \bar{r}}\right)_R \tag{26}$$

$$\frac{1}{A}\left[(1 + \alpha A B)\bar{p}_2\frac{dR}{d\tau} + \frac{R}{2}\frac{d\bar{p}_2}{d\tau}\right] = \alpha Q B(\bar{p}_2 - 1)\left(\frac{\partial \bar{c}_2}{\partial \bar{r}}\right)_R \tag{27}$$

$$\bar{u}_p = \bar{\Gamma}_p\frac{\partial \ln \bar{c}_i}{\partial \bar{r}} = \frac{\bar{\Gamma}_p}{2}\frac{\partial \ln \bar{c}_1}{\partial \bar{r}} \tag{28}$$

$$\frac{\partial \bar{n}}{\partial \tau} + \frac{1}{\bar{r}}\frac{\partial}{\partial \bar{r}}\left[\bar{r}\left(\frac{\bar{\Gamma}_p}{2}\frac{\partial \ln \bar{c}_1}{\partial \bar{r}} + \frac{R}{\bar{r}}\frac{dR}{d\tau}\right)\bar{n}\right] = \frac{\bar{D}_p}{\bar{r}}\frac{\partial}{\partial \bar{r}}\left(\bar{r}\frac{\partial \bar{n}}{\partial \bar{r}}\right) \ . \tag{29}$$

The nondimensional initial and boundary conditions are,

$$\bar{c}_1(\bar{r}, 0) = \frac{c_{1\infty}}{c_{1s}(0)} \tag{30a}$$

$$\bar{c}_1(R, \tau) = 1 \tag{30b}$$

$$\left.\frac{\partial \bar{c}_1}{\partial \bar{r}}\right|_{\bar{r}=\bar{b}} = 0 \tag{30c}$$

$$\bar{c}_2(\bar{r}, 0) = 0 \tag{30d}$$

$$\bar{c}_2(R, \tau) = 1 \tag{30e}$$

$$\left.\frac{\partial \bar{c}_2}{\partial \bar{r}}\right|_{\bar{r}=\bar{b}} = 0 \tag{30f}$$

$$\bar{p}_1(0) = 1 + \frac{\Gamma}{R(0)} = 1 + \Gamma \tag{30g}$$

$$\bar{p}_2(0) = 0 \tag{30h}$$

$$R(0) = 1 \tag{30i}$$

$$\bar{n}(\bar{r}, 0) = 1 \tag{30j}$$

$$\left.\frac{\partial \bar{n}}{\partial \bar{r}}\right|_{\bar{r}=\bar{b}} = 0 \tag{30k}$$

$$\left.\frac{\partial \bar{n}}{\partial \bar{r}}\right|_{\bar{r}=R} = 0 \quad \text{for} \quad \bar{\Gamma}_p > 0 \quad \text{and} \quad \bar{n}(R,\tau) = 0 \quad \text{for} \quad \bar{\Gamma}_p < 0 \ . \tag{30l}$$

97

For calculations in the domain $a < r < b$ or $R < \bar{r} < \bar{b}$, we rescale the equations once more with $\tilde{r} = \dfrac{\bar{r} - R}{\bar{b} - R}$. Rescaled equations (22-29) are,

$$\frac{\partial \bar{c}_1}{\partial \tau} + \frac{\bar{c}_1}{\bar{p}_1}\frac{d\bar{p}_1}{d\tau} + \frac{R}{(\bar{b}-R)[(\bar{b}-R)\tilde{r}+R]}\frac{dR}{d\tau}\frac{\partial \bar{c}_1}{\partial \tilde{r}} = \frac{1}{(\bar{b}-R)^2}\frac{\partial^2 \bar{c}_1}{\partial \tilde{r}^2} + \frac{1}{(\bar{b}-R)[(\bar{b}-R)\tilde{r}+R]}\frac{\partial \bar{c}_1}{\partial \tilde{r}} \tag{31}$$

$$\frac{\partial \bar{c}_2}{\partial \tau} + \frac{\bar{c}_2}{\bar{p}_2 - 1}\frac{d\bar{p}_2}{d\tau} + \frac{R}{(\bar{b}-R)[(\bar{b}-R)\tilde{r}+R]}\frac{dR}{d\tau}\frac{\partial \bar{c}_2}{\partial \tilde{r}} = Q\left[\frac{1}{(\bar{b}-R)}\frac{\partial^2 \bar{c}_2}{\partial \tilde{r}^2} + 1(\bar{b}-R)[(\bar{b}-R)\tilde{r}+R]\frac{\partial \bar{c}_2}{\partial \tilde{r}}\right] \tag{32}$$

$$\frac{dR}{d\tau} = \frac{\bar{p}_1\left(\frac{\partial \bar{c}_1}{\partial \tilde{r}}\right)_{\tilde{r}=0} + \alpha B Q(\bar{p}_2 - 1)\left(\frac{\partial \bar{c}_2}{\partial \tilde{r}}\right)_{\tilde{r}=0}}{\frac{(\bar{b}-R)}{A}\left(1 + \frac{\Gamma}{2R}\right) + (\bar{b}-R)(\bar{p}_1 + \alpha B \bar{p}_2)} \tag{33}$$

$$\frac{1}{A}\left[(1+A)\bar{p}_1\frac{dR}{d\tau} + \frac{R}{2}\frac{dp_1}{d\tau}\right] = \frac{\bar{p}_1}{\bar{b}-R}\left(\frac{\partial \bar{c}_1}{\partial \tilde{r}}\right)_{\tilde{r}=0} \tag{34}$$

$$\frac{1}{A}\left[(1+\alpha A B)\bar{p}_2\frac{dR}{d\tau}\frac{R}{2}\frac{d\bar{p}_2}{d\tau}\right] = \frac{\alpha Q B(\bar{p}_2 - 1)}{\bar{b}-R}\left(\frac{\partial \bar{c}_2}{\partial \tilde{r}}\right)_{\tilde{r}=0} \tag{35}$$

$$\tilde{u}_p = \frac{\bar{\Gamma}_p}{2(\bar{b}-R)}\frac{\partial \ln \bar{c}_1}{\partial \tilde{r}} \tag{36}$$

$$\frac{\partial n}{\partial \tau} + \frac{1}{(\bar{b}-R)[(\bar{b}-R)\tilde{r}+R]}\frac{\partial}{\partial \tilde{r}}\left[[(\bar{b}-R)\tilde{r}+R]\left(\frac{\bar{\Gamma}_p}{2(\bar{b}-R)}\frac{d\ln \bar{c}_1}{d\tilde{r}} + \frac{R}{[(\bar{b}-R)\tilde{r}+R]}\frac{dR}{d\tau}\right)\bar{n}\right] = \frac{\bar{D}_p}{(\bar{b}-R)[(\bar{b}-R)\tilde{r}+R]}\frac{\partial}{\partial \tilde{r}}\left[\left(\tilde{r} + \frac{R}{\bar{b}-R}\right)\frac{\partial \bar{n}}{\partial \tilde{r}}\right] \ . \tag{37}$$

The rescaled initial and boundary conditions are,

$$\bar{c}_1(\tilde{r}, 0) = \frac{c_{1\infty}}{c_{1s}(0)} \tag{38a}$$

$$\bar{c}_1(0, \tau) = 1 \tag{38b}$$

$$\frac{\partial \bar{c}_1}{\partial \tilde{r}}(1, \tau) = 0 \tag{38c}$$

$$\bar{c}_2(\tilde{r}, 0) = 0 \tag{38d}$$

$$\bar{c}_2(0, \tau) = 1 \tag{38e}$$

$$\frac{\partial \bar{c}_2}{\partial \tilde{r}}(1, \tau) = 0 \tag{38f}$$

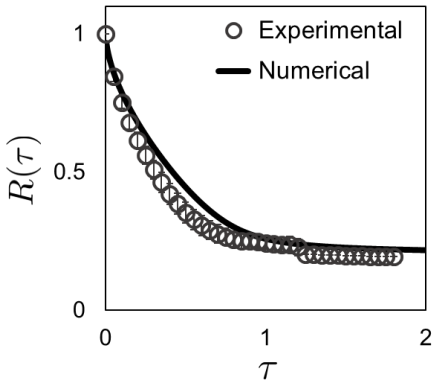

Figure S4: Nondimensional bubble radii $R(\tau)$ obtained from experiments and the model are plotted versus nondimensional time τ.

$$\bar{n}(\tilde{r},0) = 1 \tag{38g}$$

$$\left.\frac{\partial \bar{n}}{\partial \tilde{r}}\right|_{\tilde{r}=1} = 0 \tag{38h}$$

$$\left.\frac{\partial \bar{n}}{\partial \tilde{r}}\right|_{\tilde{r}=0} = 0 \ \text{ for } \ \bar{\Gamma}_p > 0 \ \text{ and } \ \bar{n}(0,\tau) = 0 \ \text{ for } \ \bar{\Gamma}_p < 0 \tag{38i}$$

$$\bar{p}_1(0) = 1 + \Gamma \tag{38j}$$

$$\bar{p}_2(0) = 0 \tag{38k}$$

$$R(0) = 1 \ . \tag{38l}$$

For a bubble with initial radius $a_0 = 2.75$ mm,[5–7]

$$\begin{aligned} &A = 0.85 \ , \ B = 0.0143 \ , \ \Gamma = 0.00024 \ , \ Q = 1.04 \ , \ \bar{b} = 4 \ , \ k_1 = 1.5 \times 10^{-5} \ \text{kg/m}^3\text{Pa} \ , \\ &k_2 = 2.15 \times 10^{-7} \ \text{kg/m}^3\text{Pa} \ , \ R_{g1} = 188.9 \ \text{J/kg K} \ , \ R_{g2} = 286.9 \ \text{J/kg K} \ , \ c_{2\infty} = k_2 p_a \ , \\ &\bar{\Gamma}_p = -0.4 \ , \ \bar{D}_p = 0.00023 \ . \end{aligned} \tag{39}$$

As a part of comparison between the model and the experiments, we first calculated (model) and measured (experiments) the radius change of the bubble $R(\tau) = a(t)/a_0$, which is plotted versus nondimensional time τ in Fig. S4. Measurements of the bubble radius change in the Hele-Shaw cell are made in three different liquid conditions (DI water, a-PS and PS particle suspensions, where pH=6-7) and the average values are plotted. There is no fitting parameter used for the model. Agreement between the model calculation and the experimental measurements suggest that the one-dimensional model accurately predicts the rate of diffusion of gases and ions. It also suggest that we are accurately predicting the position of the moving boundary, where the particles are either accumulating or being removed. The particle distribution calculated with the corresponding diffusiophoretic velocity is plotted in later section.

B. Diffusiophoresis of particles near a CO_2-permeable PDMS wall (HS-PC)

Now let's consider the second system where CO_2 dissolves into the liquid through a PDMS wall (Fig. S3(b)). The inner cell ($r = a = 3$ mm) keeps CO_2 at a constant pressure. In the experiments, the inner PDMS wall is 1-mm thick, but in the model calculations we assume that the wall has a negligible thickness. In other words, if we set CO_2 pressure at p_1, CO_2 concentration in liquid at $r = a$ is $c_{1s} = k_1 p_1$, which is a constant. For this system, we can write diffusion-reaction equations for CO_2 and ions.

$$\frac{\partial c_1}{\partial t} = \frac{D_1}{r}\frac{\partial}{\partial r}\left(r\frac{\partial c_1}{\partial r}\right) - (k_f c_i - k_r c_i^2) \tag{40}$$

$$\frac{\partial c_i}{\partial t} = \frac{D_A}{r}\frac{\partial}{\partial r}\left(r\frac{\partial c_i}{\partial r}\right) + (k_f c_1 - k_r c_i^2)\ . \tag{41}$$

Then, we can do similar scaling analysis for this model as the previous section, and decouple the CO_2 diffusion and reaction. Let

$$\bar{c}_1 = \frac{c_1}{c_{1s}}\ ,\ \bar{c}_i = \frac{c_i}{c_{is}}\ ,\ \bar{r} = \frac{r}{a}\ ,\ \bar{b} = \frac{b}{a}\ ,\ \tau = \frac{t}{a^2/D_1}\ , \tag{42}$$

then

$$(40) \Rightarrow \frac{\partial \bar{c}_1}{\partial \tau} = \frac{\partial^2 \bar{c}_1}{\partial \bar{r}^2} + \frac{1}{\bar{r}}\frac{\partial \bar{c}_i}{\partial \bar{r}} - \frac{\tau_D}{\tau_i}\left(\frac{k_f}{k_r c_{1s}}\right)^{\frac{1}{2}}(\bar{c}_1 - \bar{c}_i^2)\ , \tag{43}$$

where in this case $\tau_D = \dfrac{a^2}{D_1}$, $\tau_i = (k_r c_{is})^{-1}$ and $\left(\dfrac{k_r}{k_r c_{1s}}\right)^{\frac{1}{2}} = \dfrac{c_{is}}{c_{1s}}$. Also,

$$(41) \Rightarrow \frac{\tau_i}{\tau_D}\left[\frac{\partial \bar{c}_i}{\partial \tau} - \bar{D}_A\left(\frac{\partial^2 \bar{c}_i}{\partial \bar{r}^2} + \frac{1}{\bar{r}}\frac{\partial \bar{c}_i}{\partial \bar{r}}\right)\right] = \bar{c}_1 - \bar{c}_i^2\ . \tag{44}$$

Therefore, for $\tau_i \ll \tau_D$ and $\dfrac{c_{is}}{c_{1s}} \ll 1$ we can rewrite the equations (43) and (44) as

$$\frac{\partial \bar{c}_1}{\partial \tau} = \frac{1}{\bar{r}}\frac{\partial}{\partial \bar{r}}\left(\bar{r}\frac{\partial \bar{c}_1}{\partial \bar{r}}\right) \quad \text{and} \quad \bar{c}_1 - \bar{c}_i^2 = 0\ . \tag{45}$$

The particle distribution $n(r,t)$ in the region $a < r < b$ can be written as below with $u_p = \Gamma_p \dfrac{\partial \ln c_i}{\partial r}$,

$$\frac{\partial n}{\partial t} + \frac{1}{r}\frac{\partial}{\partial r}\left(r\Gamma_p\frac{\partial \ln c_i}{\partial r}n\right) = \frac{D_p}{r}\frac{\partial}{\partial r}\left(r\frac{\partial n}{\partial r}\right)\ . \tag{46}$$

Nondimensionalizing the particle equations with

$$\bar{n} = \frac{n}{n_0}\ ,\ \bar{D}_p = \frac{D_p}{D_1}\ ,\ \bar{\Gamma}_p = \frac{\Gamma_p}{D_1}\ , \tag{47}$$

we obtain

$$\bar{c}_i = \sqrt{\bar{c}_1} \tag{48}$$

$$\frac{\partial \bar{c}_1}{\partial \tau} = \frac{\partial^2 \bar{c}_1}{\partial \bar{r}^2} + \frac{1}{\bar{r}}\frac{\partial \bar{c}_1}{\partial \bar{r}} \tag{49}$$

$$\bar{u}_p = \bar{\Gamma}_p\frac{\partial \ln \bar{c}_1}{\partial \bar{r}} = \frac{\bar{\Gamma}_p}{2}\frac{\partial \ln \bar{c}_1}{\partial \bar{r}} \tag{50}$$

$$\frac{\partial \bar{n}}{\partial \tau} + \frac{1}{\bar{r}}\frac{\partial}{\partial \bar{r}}\left[\bar{r}\left(\frac{\bar{\Gamma}_p}{2}\frac{\partial \ln \bar{c}_1}{\partial \bar{r}}\right)\bar{n}\right] = \frac{\bar{D}_p}{\bar{r}}\frac{\partial}{\partial \bar{r}}\left(\bar{r}\frac{\partial \bar{n}}{\partial \bar{r}}\right)\ . \tag{51}$$

The nondimensional initial and boundary conditions are,

$$\bar{c}_1(\bar{r},0) = \frac{c_{1\infty}}{c_{1s}} \tag{52a}$$

$$\bar{c}_1(1,\tau) = 1 \tag{52b}$$

$$\frac{\partial \bar{c}_1}{\partial \bar{r}}(\bar{b},\tau) = 0 \tag{52c}$$

$$\bar{n}(\bar{r},0) = 1 \tag{52d}$$

$$\frac{\partial \bar{n}}{\partial \bar{r}}(\bar{b},\tau) = 0 \tag{52e}$$

$$\frac{\partial \bar{n}}{\partial \bar{r}}(1,\tau) = 0 \ \text{ for } \ \bar{\Gamma}_p > 0 \ \text{ and } \ -\bar{u}_p\bar{n}|_{\bar{r}=1} + \bar{D}_p\left.\frac{\partial \bar{n}}{\partial \bar{r}}\right|_{\bar{r}=1} = 0 \ \text{ for } \ \bar{\Gamma}_p < 0\ . \tag{52f}$$

Again, the equations can be further rescaled so that the domain of analysis becomes $0 < \hat{r} = \dfrac{\bar{r}-1}{\bar{b}-1} < 1$.

$$\bar{c}_i = \sqrt{\bar{c}_1} \tag{53}$$

$$\frac{\partial \bar{c}_1}{\partial \tau} = \frac{1}{(\bar{b}-1)^2}\frac{\partial^2 \bar{c}_1}{\partial \hat{r}^2} + \frac{1}{[(\bar{b}-1)\hat{r}+1](\bar{b}-1)}\frac{\partial \bar{c}_1}{\partial \hat{r}} \tag{54}$$

$$\frac{\partial \bar{n}}{\partial \tau} + \frac{1}{[(\bar{b}-1)\hat{r}+1]}\frac{1}{(\bar{b}-1)}\frac{\partial}{\partial \hat{r}}\left[[(\bar{b}-1)\hat{r}+1]\left(\frac{\bar{\Gamma}_p}{2}\frac{1}{(\bar{b}-1)}\frac{\partial \ln \bar{c}_1}{\partial \hat{r}}\right)\bar{n}\right]$$
$$= \frac{\bar{D}_p}{[(\bar{b}-1)\hat{r}+1]}\frac{1}{(\bar{b}-1)}\frac{\partial}{\partial \hat{r}}\left[[(\bar{b}-1)\hat{r}+1]\frac{1}{(\bar{b}-1)}\frac{\partial \bar{n}}{\partial \hat{r}}\right] . \tag{55}$$

The rescaled initial and boundary conditions are,

$$\bar{c}_1(\hat{r},0) = \frac{c_{1\infty}}{c_{1s}} \tag{56a}$$

$$\bar{c}_1(0,\tau) = 1 \tag{56b}$$

$$\frac{\partial \bar{c}_1}{\partial \hat{r}}(1,\tau) = 0 \tag{56c}$$

$$\bar{n}(\hat{r},0) = 1 \tag{56d}$$

$$\left.\frac{\partial \bar{n}}{\partial \hat{r}}\right|_{\hat{r}=0} = 0 \quad \text{for} \quad \bar{\Gamma}_p > 0 \quad \text{and} \quad -\bar{D}_p\left.\frac{\partial \bar{n}}{\partial \hat{r}}\right|_{\hat{r}=0} + \frac{\bar{\Gamma}_p}{2}\left.\frac{\partial \ln \bar{c}_1}{\partial \hat{r}}\bar{n}\right|_{\hat{r}=0} = 0 \quad \text{for} \quad \bar{\Gamma}_p < 0 \tag{56e}$$

$$\left.\frac{\partial \bar{n}}{\partial \hat{r}}\right|_{\hat{r}=1} = 0 . \tag{56f}$$

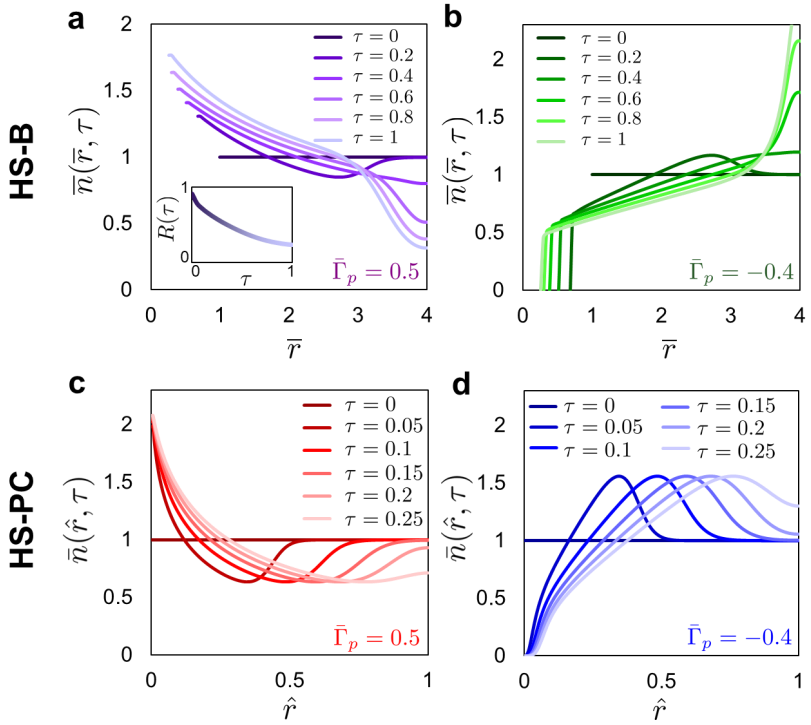

Figure S5: Particle concentration plotted versus dimensionless position for different times. (a,b) For the CO_2 bubble system, $\bar{n}(\bar{r},\tau)$ is plotted versus $\bar{r}$ for (a) positively charged particles ($\bar{\Gamma}_p = 0.5$) and (b) negatively charged particles ($\bar{\Gamma}_p = -0.4$).(a) Inset: $R(\tau)$ plotted versus τ. (c,d) For the fixed boundary system, $\bar{n}(\hat{r},\tau)$ is plotted versus $\hat{r}$ for (c) $\bar{\Gamma}_p = 0.5$ and (d) $\bar{\Gamma}_p = -0.4$. Positively charged particles show increasing particle concentration toward the CO_2 dissolving interface, whereas the concentration of negatively charged particles decrease near the interface. For all four graphs, we can obtain the nondimensional distance $\bar{r}(\bar{n}=1)$ and $\hat{r}(\bar{n}=1)$ where the nondimensional particle concentration is 1. The comparison for this length scale between model and experiments are shown in Fig. 1 in the main text.

§§ The initial condition $c_{1\infty}$

In the experiments, particle suspension was made with deionized (DI) water (Milli-Q). As the DI water is brought into atmospheric condition, CO_2 in the ambient dissolves into the water. The maximum possible concentration of CO_2 in the particle suspension is $c_{1\infty}^{\max} = k_h p_{co_2} = 1.3 \times 10^{-5}$ M, where p_{co_2} is the partial pressure of CO_2 in air ($\approx$ 40 Pa). This results in the ion concentration $c_{i\infty} = 2.4 \times 10^{-6}$ M and the pH = 5.6. However, the measured pH values of the particle suspension is pH = 6-7, suggesting smaller initial ion concentration than the maximum value. Therefore, we choose the initial condition for c_1 in all calculations to be $c_{1\infty} = 0.2 c_{1\infty}^{\max}$, which corresponds to the pH = 5.9.

Equations (31-37) and (54-55) are solved and plotted in Fig. S5-S6. We solve the coupled partial differential equations numerically with MATLAB. For the moving boundary case (equations (31-37)), we consider forward difference scheme for the entire domain with a spatial step $\delta\bar{r} = 1/100$ and a time step $\delta\tau = 10^{-4}$. For the fixed boundary case (equations (54-55)), we employ an upwinding scheme to avoid numerical instability. Thus, we apply forward and backward difference scheme for positively and negatively charged particles, respectively, with a spatial step $\delta\hat{r} = 1/100$ and a time step $\delta\tau = 10^{-4}$.

In Fig. S5, time evolution of particle distribution is plotted versus radial position for both bubble and the fixed boundary systems. In the bubble system (Fig. S5(a,b)), positively charged particles gradually accumulate at the bubble interface as the radius decreases (Fig. S5(a)). Negatively charged particles, on the other hand, are cleared away from the bubble interface and migrate toward the outer wall $\bar{r} = \bar{b}$. It is difficult to directly compare the particle distribution between the model and experiments, as the model does not consider all the experimental details. However, there is good qualitative agreement between the model and experiments in terms of particle directionality. For both moving and fixed boundary systems, and for all charges, we note from the graphs in Fig. S5 that the nondimensional positions $\bar{r}(\bar{n} = 1)$ and $\hat{r}(\bar{n} = 1)$ can be defined. These macroscopic exclusion/accumulation boundaries are also observed in experiments, in the length scales larger than the initial radius ($r = a_0$) for bubble system and the inner wall radius $r = a$ for the fixed boundary system. Therefore, we choose to compare this value directly between the model and experiments, and it is plotted versus time (τ) in Fig. 1 of the main text.

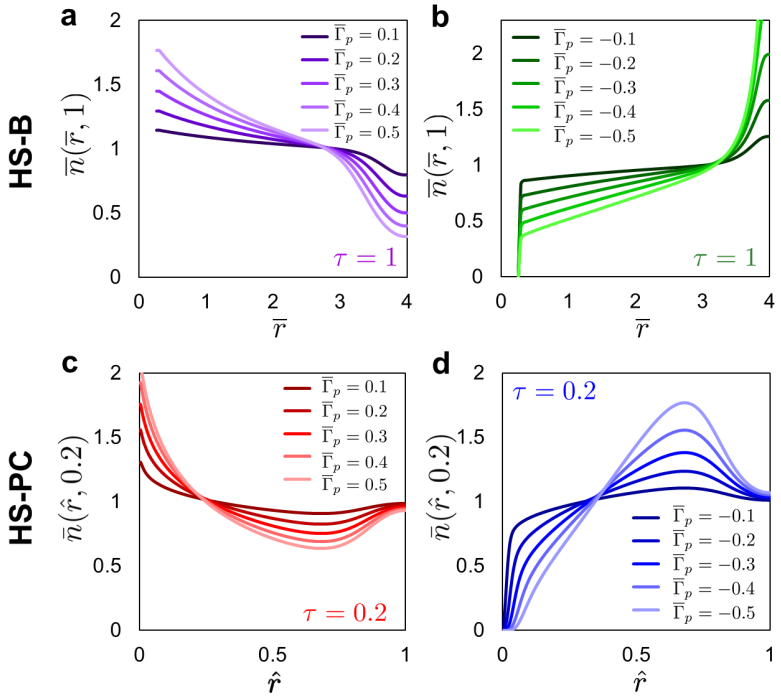

Figure S6: Effect of diffusiophoretic mobility on the particle distribution. (a,b) Particle distribution at $\tau = 1$ for different mobilities are plotted versus $\bar{r}$. (a) Positively charged particles with larger mobility accumulate more near the bubble interface, whereas (b) negatively charged particles are excluded more for larger mobilities near the bubble interface. (c,d) Particle distribution at $\tau = 0.2$ for different mobilities are plotted versus $\hat{r}$ for the fixed boundary system.

We also tested the effect of particle mobilities $\bar{\Gamma}_p$ on the particle distribution and plotted in Fig. S6. In both systems, positively charged particles with larger mobilities accumulated more near the CO_2 dissolving interface, and negatively charged particles with larger mobilities cleared more of the interfacial region. For the negatively charged particle case in the fixed boundary system, both experiments and the model calculations suggest existence of particle-free zone within $r - a \approx 200$ μm or $\hat{r} \approx 0.03$.

C. Macroscopic growth of accumulation and exclusion zone

In the experiments, we observe growing boundaries of a-PS accumulation and PS exclusion in the region $r > a_0$ for HS-B (Fig. S7(a), video 2) and $r > a$ for HS-PC (Fig. S7(b), video 3). Time evolution of detected boundaries are compared with the model in Fig. 1 in the main text. The boundaries (shown with colored arrows in Fig. S7) were detected by sharp change in local gray values.

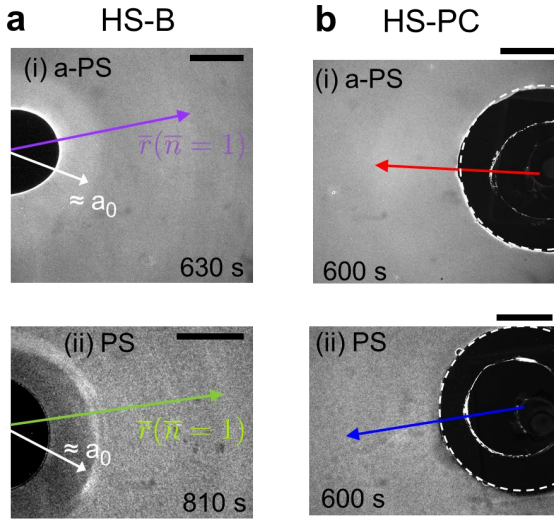

Figure S7: Growth of macroscopic accumulation and exclusion zones. (a) Experimental images showing accumulation and exclusion of particles in HS-B. There is growth of accumulation and exclusion boundaries in the region $r > a_0$. (b) Images of a-PS and PS experiments in HS-PC, showing growing of accumulation and exclusion boundaries in the region $r > a$. Scale bars are 2 mm.

D. Effect of wall diffusioosmosis on the particle velocity: side view of the Hele-Shaw cell

In order to include more details for predicting the particle behavior in the Hele-Shaw cell, we construct a model calculation that considers the side view of the system for HS-PC (Figure S8). We solve for the two-dimensional axisymmetric equations that consider CO_2 diffusion, diffusiophoresis of particles, and liquid flows induced by diffusioosmosis at the top and bottom walls.

First, we consider the equation of motion to understand the flow velocity in the Hele-Shaw cell. Let u_r and u_z be the flow velocity in r and z directions. With the axisymmetry, the azimuthal component is not included in the model calculation ($u_\theta = 0$, $\frac{\partial u_r}{\partial \theta} = \frac{\partial u_z}{\partial \theta} = 0$).

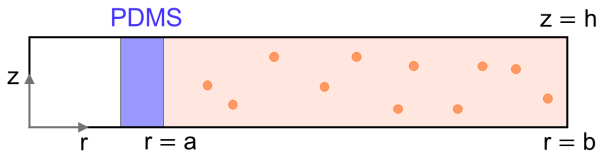

Figure S8: Schematic of the side view of a Hele-Shaw cell.

Continuity equation with the incompressible assumption is

$$\frac{1}{r}\frac{\partial(ru_r)}{\partial r}+\frac{\partial u_z}{\partial z}=0\ . \tag{57}$$

For the characteristic velocity scale in the system defined as $U_c \approx D_c/a$, Reynolds number $Re = \rho U_c a/\mu = \rho D_1/\mu \approx 0.002 \ll 1$. So we consider the Stokes equation to solve for the flow velocity in the system; $\boldsymbol{\nabla} p = \mu\nabla^2\mathbf{u}$.

$$\frac{\partial p}{\partial r}=\mu\left[\frac{1}{r}\frac{\partial}{\partial r}\left(r\frac{\partial u_r}{\partial r}\right)-\frac{u_r}{r^2}+\frac{\partial^2 u_r}{\partial z^2}\right] \tag{58}$$

$$\frac{\partial p}{\partial z}=\mu\left[\frac{1}{r}\frac{\partial}{\partial r}\left(r\frac{\partial u_r}{\partial r}\right)+\frac{\partial^2 u_r}{\partial z^2}\right]. \tag{59}$$

The advection-diffusion equation for CO_2 can be written as

$$\frac{\partial c_1}{\partial t}+u_r\frac{\partial c_1}{\partial r}+u_z\frac{\partial c_1}{\partial z}=D_1\left[\frac{1}{r}\frac{\partial}{\partial r}\left(r\frac{\partial c_1}{\partial r}\right)+\frac{\partial^2 c_1}{\partial z^2}\right]\ , \tag{60}$$

with the boundary conditions $c_1(r,z,0)=c_{1\infty},\ c_1(a,z,t)=c_{1a},\ \frac{\partial c_1}{\partial r}(b,z,t)=0$ and $\frac{\partial c_1}{\partial z}(r,0,t)=\frac{\partial c_1}{\partial z}(r,h,t)=0$. The boundary condition c_{1a} is the time dependent CO_2 concentration that is applied through the PDMS membrane. As discussed earlier, the ion concentration $c_i=\sqrt{k_f c_1/k_r}$. The diffusiophoretic velocity of particles also has two components;

$$\boldsymbol{u_p}=\Gamma_p\frac{\partial \ln c_i}{\partial r}\boldsymbol{e_r}+\Gamma_p\frac{\partial \ln c_i}{\partial z}\boldsymbol{e_z}\ . \tag{61}$$

The advection-diffusion equation for particles is

$$\frac{\partial n}{\partial t}+\frac{1}{r}\frac{\partial}{\partial r}\left[r\left(u_r+\Gamma_p\frac{\partial \ln c_i}{\partial r}\right)n\right]+\frac{\partial}{\partial z}\left[\left(u_z+\Gamma_p\frac{\partial \ln c_i}{\partial z}\right)n\right]=D_p\left[\frac{1}{r}\frac{\partial}{\partial r}\left(r\frac{\partial n}{\partial r}\right)+\frac{\partial^2 n}{\partial z^2}\right]\ , \tag{62}$$

and the boundary conditions are, $n(r,z,0)=n_0$, $\frac{\partial n}{\partial r}(a,z,t)=0$ for $\Gamma_p>0$, $\Gamma_p\frac{\partial \ln c_i}{\partial r}n-D_p\frac{\partial n}{\partial r}=0$ for $\Gamma_p<0$ at $r=a$, $\frac{\partial n}{\partial r}(b,z,t)=0$, and $\frac{\partial n}{\partial z}(r,0,t)=\frac{\partial n}{\partial z}(r,h,t)=0$.

Now we nondimensionalize the equations for the convenience of numerical calculations. For this configuration we choose h as the characteristic length scale (we present the comparison among experiments, model and the experiments in the main text in dimensional form). Define the nondimensional variables as

$$\bar{\bar{r}}=\frac{r}{h}\ ,\quad \bar{z}=\frac{z}{h}\ ,\quad \bar{\tau}=\frac{t}{h^2/D_1}\ ,\quad \bar{\bar{u}}_r=\frac{u_r}{D_1/h}\ ,\quad \bar{\bar{u}}_z=\frac{u_z}{D_1/h}\ ,\quad \bar{\bar{u}}_p=\frac{u_p}{D_1/h}\ ,\quad \bar{c}_1=\frac{c_1}{c_{1s}}\ ,\quad \bar{c}_i=\frac{c_i}{c_{is}}\ ,$$

$$\bar{n}=\frac{n}{n_0}\ ,\quad \bar{\bar{a}}=\frac{a}{h}\ ,\quad \bar{\bar{b}}=\frac{b}{h}\ ,\quad \bar{p}=\frac{p}{\mu D_1/h^2}\ .$$

Then,

$$\frac{\partial \bar{p}}{\partial \bar{\bar{r}}}=\frac{1}{\bar{\bar{r}}}\frac{\partial}{\partial \bar{\bar{r}}}\left(\bar{\bar{r}}\frac{\partial \bar{\bar{u}}_r}{\partial \bar{\bar{r}}}\right)-\frac{\bar{\bar{u}}_r}{\bar{\bar{r}}^2}+\frac{\partial^2 \bar{\bar{u}}_r}{\partial \bar{z}^2} \tag{63}$$

$$\frac{\partial \bar{p}}{\partial \bar{z}}=\frac{1}{\bar{\bar{r}}}\frac{\partial}{\partial \bar{\bar{r}}}\left(\bar{\bar{r}}\frac{\partial \bar{\bar{u}}_z}{\partial \bar{\bar{r}}}\right)+\frac{\partial^2 \bar{\bar{u}}_z}{\partial \bar{z}^2}\ . \tag{64}$$

The nondimensional continuity equation is

$$\frac{\partial(\bar{\bar{r}}\bar{\bar{u}}_r)}{\partial \bar{\bar{r}}}+\frac{\partial(\bar{\bar{r}}\bar{\bar{u}}_z)}{\partial \bar{z}}=0 \tag{65}$$

Equations for CO_2 and ion concentrations are

$$\frac{\partial \bar{c}_1}{\partial \bar{\tau}}+\bar{\bar{u}}_r\frac{\partial \bar{c}_1}{\partial \bar{z}}=\frac{1}{\bar{\bar{r}}}\frac{\partial}{\partial \bar{\bar{r}}}\left(\bar{\bar{r}}\frac{\partial \bar{c}_1}{\partial \bar{\bar{r}}}\right)+\frac{\partial^2 \bar{c}_1}{\partial \bar{z}^2}\ ,\quad \bar{c}_i=\sqrt{\bar{c}_1}\ , \tag{66}$$

and $\bar{c}_1(\bar{\bar{r}},\bar{z},0)=\frac{p_{co_2}}{p_1}$, $\bar{c}_1(\bar{\bar{a}},\bar{z},\bar{\tau})=\bar{c}_{1a}$, $\frac{\partial\bar{c}_1}{\partial\bar{\bar{r}}}(\bar{\bar{b}},\bar{z},\bar{\tau})=0$, and $\frac{\partial\bar{c}_1}{\partial\bar{z}}(\bar{\bar{r}},0,\bar{\tau})=\frac{\partial\bar{c}_1}{\partial\bar{z}}(\bar{\bar{r}},1,\bar{\tau})=0$.

The particle equation is

$$\frac{\partial\bar{n}}{\partial\bar{\tau}}+\frac{1}{\bar{\bar{r}}}\frac{\partial}{\partial\bar{\bar{r}}}\left[\bar{\bar{r}}\left(\bar{\bar{u}}_r+\frac{\bar{\Gamma}_p}{2}\frac{\partial\ln\bar{c}_1}{\partial\bar{\bar{r}}}\right)\bar{n}\right]+\frac{\partial}{\partial\bar{z}}\left[\left(\bar{\bar{u}}_z+\frac{\bar{\Gamma}_p}{2}\frac{\partial\ln\bar{c}_1}{\partial\bar{z}}\right)\bar{n}\right]=\bar{D}_p\left[\frac{1}{\bar{\bar{r}}}\frac{\partial}{\partial\bar{\bar{r}}}\left(\bar{\bar{r}}\frac{\partial\bar{n}}{\partial\bar{\bar{r}}}\right)+\frac{\partial^2\bar{n}}{\partial\bar{z}^2}\right]\ . \tag{67}$$

Boundary conditions are, $\bar{n}(\bar{\bar{r}},\bar{z},0)=1$, $\frac{\partial\bar{n}}{\partial\bar{\bar{r}}}(\bar{\bar{a}},\bar{z},\bar{\tau})=0$ for $\bar{\Gamma}_p>0$, $\frac{\bar{\Gamma}_p}{2}\frac{\partial\ln\bar{c}_1}{\partial\bar{\bar{r}}}\bar{n}-\bar{D}_p\frac{\partial\bar{n}}{\partial\bar{\bar{r}}}=0$ for $\bar{\Gamma}_p<0$ at $\bar{\bar{r}}=\bar{\bar{a}}$, $\frac{\partial\bar{n}}{\partial\bar{\bar{r}}}(\bar{\bar{b}},\bar{z},\bar{\tau})=0$, and $\frac{\partial\bar{n}}{\partial\bar{z}}(\bar{\bar{r}},0,\bar{\tau})=\frac{\partial\bar{n}}{\partial\bar{z}}(\bar{\bar{r}},1,\bar{\tau})=0$.

The equations of motion can be converted to the vorticity equation by (63)$\times\frac{\partial}{\partial\bar{z}}$ − (64)$\times\frac{\partial}{\partial\bar{\bar{r}}}$, since the vorticity $\bar{\omega}=\frac{\partial\bar{\bar{u}}_r}{\partial\bar{z}}-\frac{\partial\bar{\bar{u}}_z}{\partial\bar{\bar{r}}}$. With some algebra, we obtain

$$\frac{\partial^2\bar{\omega}}{\partial\bar{\bar{r}}^2}+\frac{1}{\bar{\bar{r}}}\frac{\partial\bar{\omega}}{\partial\bar{\bar{r}}}-\frac{\bar{\omega}}{\bar{\bar{r}}^2}+\frac{\partial^2\bar{\omega}}{\partial\bar{z}^2}=0 \tag{68}$$

We can define the stream function $\bar{\psi}(\bar{\bar{r}},\bar{z})$ so to satisfy the incompressibility assumption (65), and thus

$$\bar{\bar{u}}_r=-\frac{1}{\bar{\bar{r}}}\frac{\partial\bar{\psi}}{\partial\bar{z}}\quad\text{and}\quad\bar{\bar{u}}_z=\frac{1}{\bar{\bar{r}}}\frac{\partial\bar{\psi}}{\partial\bar{\bar{r}}}\ . \tag{69}$$

Then the definition of vorticity $\bar{\omega}$ can be written with $\bar{\psi}$ as

$$\bar{\omega}=-\frac{1}{\bar{\bar{r}}}\left(\frac{\partial^2\bar{\psi}}{\partial\bar{z}^2}+\frac{\partial^2\bar{\psi}}{\partial\bar{\bar{r}}^2}\right)\ . \tag{70}$$

$\bar{\psi}=$ constant at all walls and we set $\bar{\psi}=0$. Also, on the top and bottom walls, there is diffusioosmotic slip generated by the ion concentration gradient. The corresponding boundary condition is, $\frac{\partial\bar{\psi}}{\partial\bar{z}}\big|_{\bar{z}=0,\bar{z}=1}=\frac{\bar{\Gamma}_w\bar{\bar{r}}}{2}\frac{\partial\ln\bar{c}_c}{\partial\bar{\bar{r}}}$, where $\bar{\Gamma}_w$ is the diffusioosmosis constant for the wall that is equivalent to the diffusiophoretic mobility. We chose $\bar{\Gamma}_w=-0.3$ ($\Gamma_w\approx-600\ \mu\text{m}^2/\text{s}$) to represent the glass surface in contact with the aqueous phase. The discrete boundary conditions for (70) – for numerical calculations – can be computed with a second-order Taylor series expansion of the stream function.[8]

We further shift the coordinate as $\hat{\bar{r}}=\bar{\bar{r}}-\bar{\bar{a}}$ so that the origin is at $\bar{\bar{a}}$.

The equations for CO_2 and ions are

$$\frac{\partial\bar{c}_1}{\partial\bar{\tau}}+\bar{\bar{u}}_r\frac{\partial\bar{c}_1}{\partial\bar{\bar{r}}}+\bar{\bar{u}}_z\frac{\partial\bar{c}_1}{\partial\bar{z}}=\frac{1}{\hat{\bar{r}}+\bar{\bar{a}}}\frac{\partial}{\partial\hat{\bar{r}}}\left((\hat{\bar{r}}+\bar{\bar{a}})\frac{\partial\bar{c}_1}{\partial\hat{\bar{r}}}\right)+\frac{\partial^2\bar{c}_1}{\partial\bar{z}^2}\ ,\quad\bar{c}_i=\sqrt{\bar{c}_1}\ , \tag{71}$$

and $\bar{c}_1(\hat{\bar{r}},\bar{z},0)=\frac{p_{co_2}}{p_1}$, $\bar{c}_1(0,\bar{z},\bar{\tau})=\bar{c}_{1a}$, $\frac{\partial\bar{c}_1}{\partial\hat{\bar{r}}}(\ell,\bar{z},\bar{\tau})=0$, and $\frac{\partial\bar{c}_1}{\partial\bar{z}}(\hat{\bar{r}},0,\bar{\tau})=\frac{\partial\bar{c}_1}{\partial\bar{z}}(\hat{\bar{r}},1,\bar{\tau})=0$. Note that $\ell=\bar{\bar{b}}-\bar{\bar{a}}$.

The particle equation is

$$\frac{\partial\bar{n}}{\partial\bar{\tau}}+\frac{1}{\hat{\bar{r}}+\bar{\bar{a}}}\frac{\partial}{\partial\hat{\bar{r}}}\left[(\hat{\bar{r}}+\bar{\bar{a}})\left(\bar{\bar{u}}_r+\frac{\bar{\Gamma}_p}{2}\frac{\partial\ln\bar{c}_1}{\partial\hat{\bar{r}}}\right)\bar{n}\right]+\frac{\partial}{\partial\bar{z}}\left[\left(\bar{\bar{u}}_z+\frac{\bar{\Gamma}_p}{2}\frac{\partial\ln\bar{c}_1}{\partial\bar{z}}\right)\bar{n}\right]=\bar{D}_p\left[\frac{1}{\hat{\bar{r}}+\bar{\bar{a}}}\frac{\partial}{\partial\hat{\bar{r}}}\left((\hat{\bar{r}}+\bar{\bar{a}})\frac{\partial\bar{n}}{\partial\hat{\bar{r}}}\right)+\frac{\partial^2\bar{n}}{\partial\bar{z}^2}\right]\ , \tag{72}$$

and the boundary conditions are $\bar{n}(\hat{\bar{r}},\bar{z},0)=1$, $\frac{\partial\bar{n}}{\partial\hat{\bar{r}}}(0,\bar{z},\bar{\tau})=0$ for $\bar{\Gamma}_p>0$, $\frac{\bar{\Gamma}_p}{2}\frac{\partial\ln\bar{c}_1}{\partial\hat{\bar{r}}}\bar{n}-\bar{D}_p\frac{\partial\bar{n}}{\partial\hat{\bar{r}}}=0$ for $\bar{\Gamma}_p<0$ at $\hat{\bar{r}}=0$, $\frac{\partial\bar{n}}{\partial\hat{\bar{r}}}(\ell,\bar{z},\bar{\tau})=0$, and $\frac{\partial\bar{n}}{\partial\bar{z}}(\hat{\bar{r}},0,\bar{\tau})=\frac{\partial\bar{n}}{\partial\bar{z}}(\hat{\bar{r}},1,\bar{\tau})=0$.

The vorticity equation is now

$$\frac{\partial^2\bar{\omega}}{\partial\hat{\bar{r}}^2}+\frac{1}{\hat{\bar{r}}+\bar{\bar{a}}}\frac{\partial\bar{\omega}}{\partial\hat{\bar{r}}}-\frac{\bar{\omega}}{(\hat{\bar{r}}+\bar{\bar{a}})^2}+\frac{\partial^2\bar{\omega}}{\partial\bar{z}^2}=0\ , \tag{73}$$

and

$$\bar{\omega}=-\frac{1}{\hat{\bar{r}}+\bar{\bar{a}}}\left(\frac{\partial^2\bar{\psi}}{\partial\hat{\bar{r}}^2}+\frac{\partial^2\bar{\psi}}{\partial\bar{z}^2}\right)\ . \tag{74}$$

We solve the equations (71-74) numerically with Matlab similar to the one-dimensional problems studied above. We consider upwinding scheme for solving $\bar{c}_1$ and $\bar{n}$, and thus employ forward and backward differences for positive and negative $\bar{\Gamma}_p$. For $\bar{\omega}$ and $\bar{\psi}$ we employ central difference scheme to avoid numerical instabilities, and the equation (74) is solved iteratively at each time step using the successive over-relaxation (SOR)[8] with the relaxation factor 0.9.

E.1. Concentration of CO_2 at $r = a$

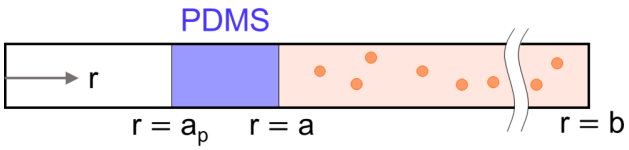

Figure S9: Schematic of a part of the Hele-Shaw cell.

In order to consider the time-dependent boundary condition for CO_2, we consider the one-dimensional radial diffusion of CO_2 in the PDMS membrane. Let the inner radius of the inner PDMS wall a_p, and the constant CO_2 pressure p_1 is applied at $r = a_p$ (Figure S9).

Let c_1^p, D_1^p ($= 2.4 \times 10^{-9}$ m^2/s) and k_h^p ($= 6.7 \times 10^{-7}$ mol/Pa·L) the concentration, diffusivity and Henry's law constant of CO_2 in PDMS,[9,10] respectively. Then for $a_p < r < a$

$$\frac{\partial c_1^p}{\partial t} = \frac{D_1^p}{r}\frac{\partial}{\partial r}\left(r\frac{\partial c_1^p}{\partial r}\right) , \tag{75}$$

and $c_1^p(r,0) = 0.2k_h^p p_{co_2}$ and $c_1^p(a_p,t) = k_h^p p_1$.

Then on the liquid side,

$$\frac{\partial c_1}{\partial t} = \frac{D_1}{r}\frac{\partial}{\partial r}\left(r\frac{\partial c_1}{\partial r}\right) , \tag{76}$$

and $c_1(r,0) = 0.2k_h p_{co_2}$ and $\frac{\partial c_1}{\partial r}\big|_b = 0$. At $r = a$, $-D_1^p \frac{\partial c_1^p}{\partial r}\big|_a = -D_1 \frac{\partial c_1}{\partial r}\big|_a$ and $\frac{c_c^p}{k_h^p} = \frac{c_c}{k_h}$.

By nondimensionalizing the equations with

$$\bar{c}_1^p = \frac{c_1^p}{k_h p_1} , \quad \bar{c}_1 = \frac{c_1}{k_h p_1} , \quad \bar{D}_1^p = \frac{D_1^p}{D_1} , \quad \tilde{\bar{r}} = \frac{r}{a_p} , \quad \tilde{\bar{a}} = \frac{a}{a_p} , \tag{77}$$

and solving the coupled equations numerically with Matlab, we obtain the time-dependent boundary condition c_{1a} that is used in the 2D calculations (Figure S10).

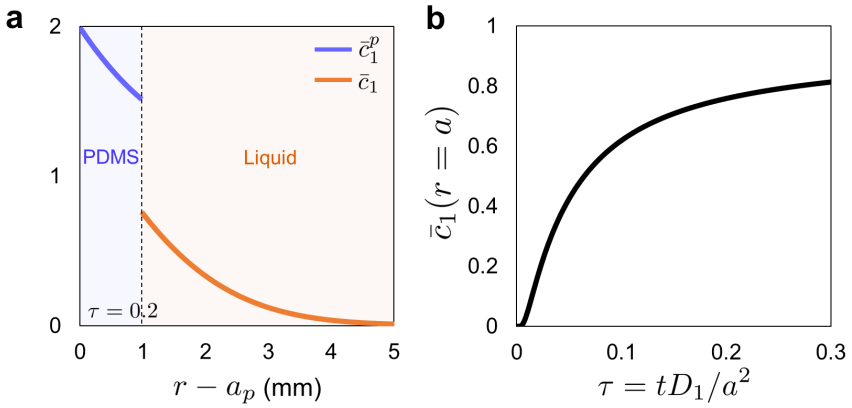

Figure S10: (a) CO_2 concentration in PDMS and in the liquid at $\tau = 0.2$. (b) CO_2 concentration in the liquid phase at $r = a$ plotted versus τ.

The radial particle velocity $\left(-\frac{1}{\tilde{\bar{r}}}\frac{\partial \bar{\psi}}{\partial \bar{z}} + \frac{\bar{\Gamma}_p}{2}\frac{\partial \ln \bar{c}_1}{\partial \tilde{\bar{r}}}\right)$ at $z = h/2$ (the velocity is further rescaled for comparison), at the radial position between $r - a \approx$ 200-600 μm is calculated and plotted versus time, and compared with the one-dimensional calculation and the experimental measurements. Below we included contour plots for the nondimensional stream function and particle concentration at two different times. Due to the diffusioosmotic flow along the wall, there is fluid flow created in the Hele-Shaw cell, and the negatively charged particles are excluded by the largest radial distance at $z = h/2$ (due to the symmetry).

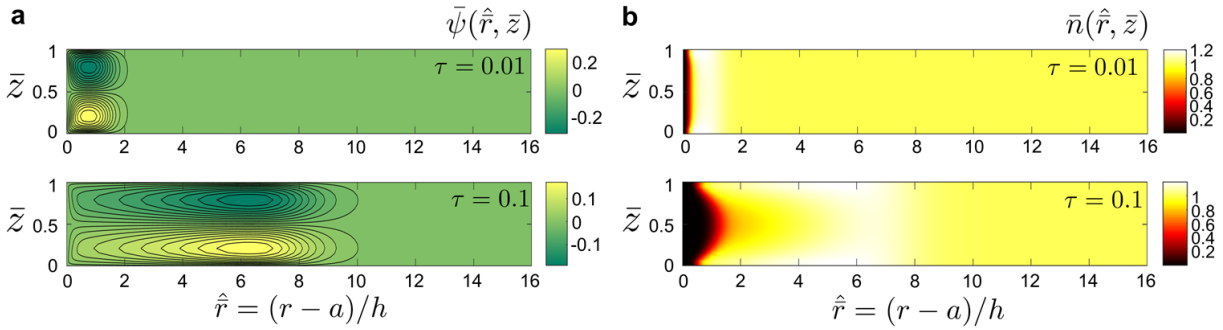

Figure S11: Contour plots obtained at two different times ($\tau = 0.01$ and 0.1) for (a) the nondimensional stream function and (b) the nondimensional particle concentration.

E.2. Early time radial diffusiophoresis in the Hele-Shaw cell

In the main text, the radial particle velocities are compared among one- and two dimensional models, particle tracking and PIV. With the constant pressure boundary condition in the one-dimensional model, the largest concentration gradient is obtained at $\tau = 0$, and the particle velocity decreases over time. The two-dimensional calculation considering time-evolving boundary condition (section I.E.1) shows increase then decrease in the radial velocities, which is also observed from the particle tracking. The two-dimensional calculation predicts higher particle speed than the measurements, and we interpret that this difference in the magnitude arises from the three-dimensional complexity in the flow near the wall. The calculation is not highly resolved to include all details of the corner flows that affect the particle motion and velocity measurements.

We are aware of possible variation of the diffusiophoretic mobility in the system[11] as the ion concentration and the Debye length change over time. Also, the zeta potential of polystyrene is expected to change under the low pH conditions.[12] However, the range of ion concentrations (and pH) we use in the experiments is small to expect dramatic change in the diffusiophoretic mobility, and the constant mobility is a reasonable assumption in our model calculations. Therefore, for the current study we conclude that the difference in the magnitude of calculated and measured velocities is due to the three-dimensional complexity in the wall region at early times. We are working to understand details of such flow structure and thus do not include in this study.

II. Bacterial strains used in the current study

We present the strain information in Table S1.

Strains/plasmid	Relevant Features	Reference
E. coli		
S17 λ-*pir*	Wild Type	
V. cholerae		
C6706*str*2	El Tor Wild Type	1
JY019	*lacZ*:P$_{tac}$-*mKO*:*lacZ*	This study
JY238	Δ*flaA lacZ*:P$_{tac}$-*mKO*:*lacZ*	This study
Plasmid		
pKAS32	Suicide vector, Amp^R Sm^S	2
pCN005	pKAS32 *lacZ*:P$_{tac}$-*mKO*:*lacZ*	13
pBH050	pKAS32 Δ*flaA*	14

Table S1: *E. coli* and *V. cholerae* strains used in this study.

III. *V. cholerae* cells in the fixed boundary system (HS-PC)

We present fluorescent images of *V. cholerae* wild-type and Δ*flaA* cells in the HS-PC system. We observe that at $\tau = 1$ which corresponds to $t \approx 75$ minutes, number of bacterial cells significantly decreased in the vicinity of CO_2 source (Fig. S12).

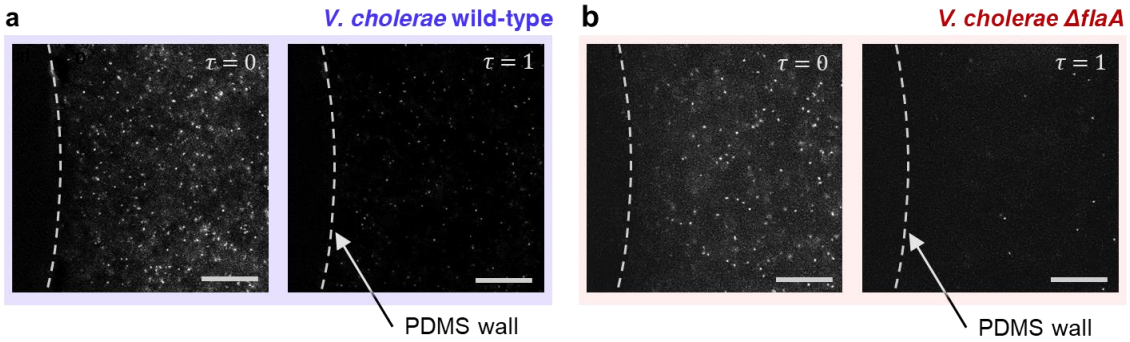

Figure S12: Fluorescent images of *V. cholerae* (a) wild-type, and (b) Δ*flaA* in the HS-PC system taken at different times. Scale bar is 50 μm.

We also present the intensity measurements from the experiments with *V. cholerae* cells in HS-B and HS-PC systems below. Decrease in the fluorescent intensity is clearly observed for both HS-B and HS-PC systems in the presence of CO_2 dissolution. We note that the background fluorescent signal from the surrounding liquid (mKO released by dead cells) has a small contribution to the intensity measurements. This suggests possible diffusiophoresis of fluorescent proteins[15] in the background liquid, since proteins carry a net surface charge away from the isoelectric point (pI). This is discussed in the next section.

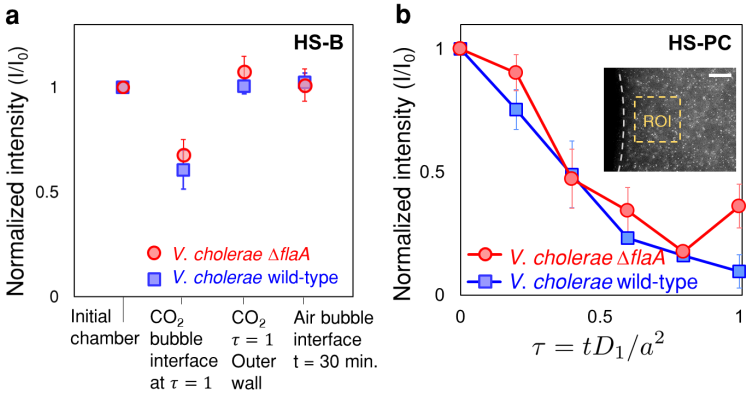

Figure S13: Intensity measurements for the selected region of interest (100 μm $\times$ 100 μm ROI, located $\approx$ 20 μm away from the interface). (a) Normalized intensity plotted for different positions and times in HS-B. A significant decrease in intensity is measured near the dissolving CO_2 bubble at $\tau = 1$. I_0 is the mean gray value of the ROI in the image at $\tau = 0$. (b) Normalized intensity near the CO_2 source plotted versus τ for HS-PC. Inset: a fluorescent image of the cells ($\Delta flaA$) in HS-PC. Scale bar is 50 μm.

IV. Suspension of bacterial cells in 10 % M9 minimal salt solution

As described in the Methods section, we suspend bacterial cells in 10 % M9 solution. The hypotonic environment excludes the unknown effects of background ions[16] and the no nutrient condition suppresses biological process of the cell. One can ask cell lysis and survival rate during the experiments. Our experimental time was less than 1 hr for *V. cholerae*, $\approx$ 30 min. for *S. aureus*, and maximum 12 hr for *P. aeruginosa*. Motile bacterial cells were found swimming both before and after the experiments.

After experiments, we collected the sample from the Hele-Shaw cell, and suspended $\approx$ 0.1 mL of the collected liquid in LB. Then the bacterial cells were regrown in LB for 24 hr (with shaking at 37 °C)and OD_{600} values were measured (Table S2). *S. aureus* was regrown for 16 hr.

V. cholerae that was used for 1 hr in HS-PC and collected at $t = 1$ hr, and *P. aeruginosa* that was used for 1 hr CO_2 exposure in HS-PC and collected at $t = 12$ hr, were regrown in LB for 24 hours with shaking at 37 °C. Then following the main protocol (Methods), the centrifuged pellet was resuspended in M9 for 2 hr (at 37 °C with shaking) and then in 10 % M9 for another set of diffusiophoresis experiments in HS-PC. The regrown cells showed diffusiophoretic motion under CO_2 gradient, and we conclude that our experimental conditions using dilute medium does not damage or change the relevant cell properties (surface charge, length scales, etc.) significantly.

Next, we discuss the influence of lysed cells in our experiments with fluorescence microscopy. In our *V. cholerae* experiments, most of the fluorescent signal comes from mKO. We note that by using 10 % M9 solution

Strain	Experiment condition	OD_{600} after 24 hr growth in LB
V. cholerae	20 min. exposure to CO_2 in HS-PC	1.94
V. cholerae	1 hr exposure to CO_2 in HS-PC	1.92
P. aeruginosa	20 min. exposure to CO_2	1.98
P. aeruginosa	1 hr exposure to CO_2 in HS-PC	1.93
P. aeruginosa	1 hr exposure to CO_2 in HS-PC, collected at $t = 12$ hr	1.94
P. aeruginosa	no CO_2 exposure, collected at $t = 12$ hr	1.94
S. aureus	20 min. exposure to CO_2 in HS-PC	OD_{600} after 16 hr growth $\approx$ 2.2

Table S2: Growth test of collected samples after different CO_2-driven diffusiophoresis experiments.

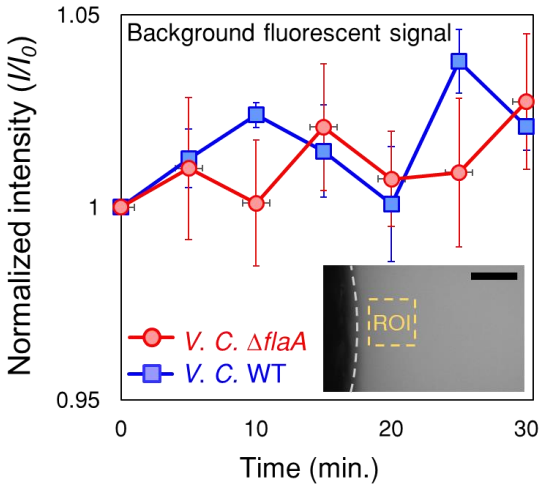

Figure S14: Fixed boundary experiments (HS-PC) for the background (filtered) solution. Normalized intensity near the CO_2 source is plotted versus time for filtered bacterial suspensions. The background fluorescent signal is expected to come from released mKO protein from lysed cells, and change in the intensity demonstrate combined behavior of mKO dispersion and diffusiophoresis. Inset: a fluorescent image of filtered solution near the CO_2 source (HS-PC). Scale bar is 100 μm.

(pH $\approx$ 6.5), some cells lyse and release cell materials into the liquid, and mKO is also expected to be released into the liquid phase where it emits fluorescent signals. One hour after making the bacterial suspension, we filtered the solution first through 200 nm, then a 20 nm filter. The filtered solution is collected for additional fixed boundary experiments (HS-PC), and we observe a slight increase in the intensity (Fig. S14) near the CO_2 source. mKO is O(1-10) nm in size, and has a surface charge that depends on pH, since proteins carry a net positive charge below the isoelectric point (pI). To the best of our knowledge, there is no literature that measured or calculated the pI of mKO, which open source pI calculators[17–19] suggest range between pI = 6.3-7.1. Therefore, our measurements in Fig. S14 must be combined dispersion and diffusiophoresis of mKO molecules in the liquid. We investigate the diffusiophoresis of mKO in.[15]

In order to examine cell lysis and denaturation of the fluorescent protein mKO, we kept the bacterial suspension for 24 hours then obtained fluorescent images under identical imaging condition (Fig. S15). We observe that the wild-type *V. cholerae* cells die over time and release fluorescent material into the surrounding liquid. The background fluorescence signal shows that mKO does not denature in the surrounding liquid.

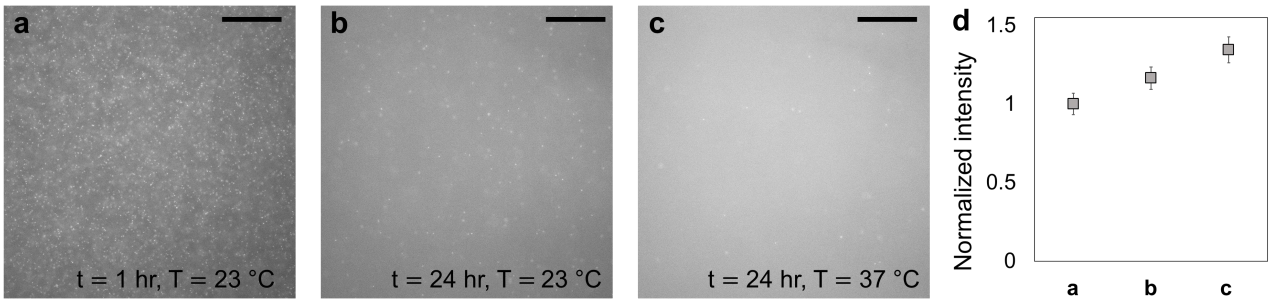

Figure S15: Bacterial suspension of wild-type *V. cholerae* cells in 10 % M9 solution. (a) 1 hour after making the experimental solution (OD_{600} = 0.23). (b) 24 hour after making the solution. The sample was kept under T = 23 °C. (c) 24 hour after making the solution. The sample was kept under T = 37 °C. (d) Normalized intensities for (a-c). Scale bars are 100 μm. The gray values are normalized by that of (a).

V. Long time behavior of a-PS and PS particles in the bubble system

To visualize the long term dynamics of a-PS and PS particles after the concentration gradient of CO_2 is removed, we performed particle experiments with a CO_2 bubble in the Hele-Shaw cell (Fig. S16). We observe that the particle distribution at $t \approx 1$ hr is maintained at $t \approx 16$ hr, due to small particle diffusivity D_p.

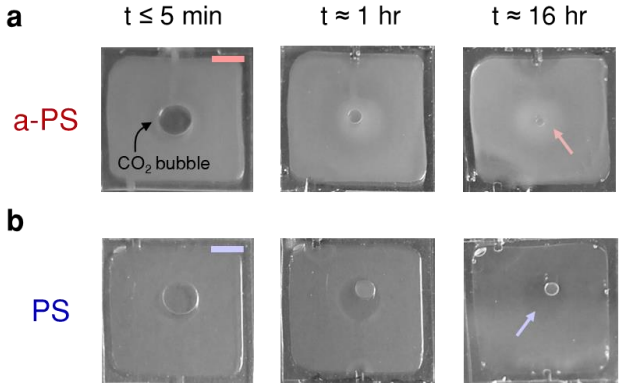

Figure S16: Distribution of a-PS and PS particles near CO_2 bubbles in the Hele-Shaw cell. Diffusiophoretic accumulation and exclusion of particles near the bubble interface are maintained for $t \geq 16$ hours due to small particle diffusivity.

VI. Long time ($t = 12$ hr) distribution of *P. aeruginosa* cells in the fixed boundary system

We present fluorescent images obtained at $t = 12$ hr for the fixed boundary experiments of *P. aeruginosa* with and without CO_2 source. As predicted and visualized in the main text (Fig. 4), after 1 hr of diffusiophoresis experiments, cells are removed from the inner PDMS wall (Fig. S17(a-i,c-i)). Without CO_2 cells are concentrated near both inner and outer PDMS walls for air source (Fig. S17(a-ii,c-ii)). These cell distributions are maintained at $t = 12$ hr.

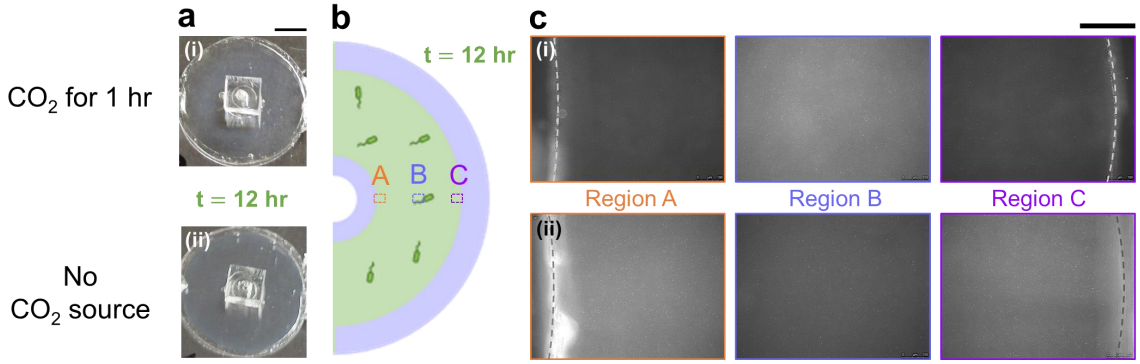

Figure S17: Long time behavior of *P. aeruginosa* after diffusiophoresis. (a) Images of the Hele-Shaw cells at $t = 12$ hr (a-i) after 1 hr CO_2-driven diffusiophoresis and (a-ii) without CO_2. (b) Schematic showing fluorescent imaging positions. (c) Fluorescent images obtained (at $t = 12$ hr) with an identical imaging condition for two systems. Cell density is visualized by different fluorescent intensities at different regions of the Hele-Shaw cell. Scale bar is 20 μm.

VII. Diffusiophoresis of motile cells

As mentioned in the main text, diffusiophoresis of motile cells is different from that of polystyrene particles or immotile cells. In our experiments, wild-type *V. cholerae* and *P. aeruginosa* are motile cells with single flagellum.[20–22] At different conditions, swimming speed of *V. cholerae* and *P. aeruginosa* are measured in the Hele-Shaw cell. We selected meandering trajectories with tracked duration longer than 1 s (Table S3). In 10 % M9 solutions, *V. cholerae* cells are slowed down compared to the reported speed (75.4 ± 9.4 μm/s),[20] due to low Na^+ concentration and room temperature condition (23 °C).[23,24] Without CO_2, the effective diffusivities of swimming cells can be estimated as $D_{\text{eff}} \approx v_t^2 t_r$ (≈ 300 μm^2/s for *V. cholerae* and $\approx$ 500-1000 μm^2/s for *P. aeruginosa* calculated with the transit time ≈ 0.56 s.[22] These values are either comparable to the estimated diffusiophoretic mobility of the cells or larger, and thus simple comparison between Γ_p and D_{eff} does not inform diffusiophoresis. In video 5, we present two movies obtained under fluorescent (10 s interval) and bright field (105 ms interval) conditions. It is observed that the flow of cells is a slow-advection with estimated Péclet number $Pe = \frac{u_p \ell_{\text{cell}}}{D_{\text{eff}}} \approx 10^{-3}$-$10^{-2}$, which means that the cells swim with their characteristic velocity, with a slow drift due to diffusiophoresis.

Strain	Tracking condition	Speed
V. cholerae	No CO_2	25.6 ± 8.9 μm/s
P. aeruginosa	No CO_2	50.37 ± 17.14 μm/s
P. aeruginosa	$t = 20$ min.	51.78 ± 11.85 μm/s
P. aeruginosa	$t = 1$ hr (CO_2 on for 1 hr)	34.87 ± 9.12 μm/s
P. aeruginosa	$t = 12$ hr (CO_2 on for first 1 hr)	31.06 ± 9.43 μm/s

Table S3: Swimming speed measurements for *V. cholerae* and *P. aeruginosa*.

We note that the typical swimming speed of *P. aeruginosa* decrease after 1 hr of CO_2 dissolution, and it may be due to the pH change affecting flagellar motor.[25] Detailed investigation of swimming patterns of *V. cholerae* and *P. aeruginosa* is not included in the current study.

References

[1] S. Shim, J. Wan, S. Hilgenfeldt, P. D. Panchal, H. A. Stone, Dissolution without disappearing: multicomponent gas exchange for CO_2 bubbles in a microfluidic channel. *Lab Chip* **14**, 2428-2436 (2014)

[2] S. Shim, Interfacial flows with Heat and Mass Transfer. (PhD Thesis, 2017, Princeton Univ.)

[3] S. Shin, O. Shardt, P. B. Warren, H. A. Stone, Membraneless water filtration using CO_2. *Nat. Comm.* **8,** 15181 DOI: 10.1038/ncomms15181 (2017)

[4] D. C. Prieve, J. L. Anderson, J. P. Ebel, M. E. Lowell, Motion of a particle generated by chemical gradients. Part 2. Electrolytes. *J. Fluid Mech.* **148,** 247-269 (1984)

[5] W. M. Haynes, *CRC Handbook of Chemistry and Physics* (CRC Press, 2015), 96th edn.

[6] C. L. Yaws, *Handbook of Properties for Environmental and Green Engineering*, 1st edn., Gulf Publishing Company (2008)

[7] W. L. Jolly, *Modern Inorganic Chemistry* (McGraw-Hill, New York, 1991), 2nd edn.

[8] S. E. Battat, Transport of Colloidal Particles by Diffusiophoresis. (Senior Thesis, 2017, Princeton Univ.)

[9] T. C. Merkel, V. I. Bondar, K. Nagai B. D. Freeman, I. Pinnau, Gas sorption, diffusion, and permeation in poly(dimethylsiloxane), *J. Polym. Sci. B* **38,** 415-434 (2000)

[10] S. G. Charati and S. A. Stern, Diffusion of gases in silicone polymers: Molecular dynamics simulations, *Macromolecules*, **31,** 5529-5535 (1998)

[11] A. Gupta, S. Shim, and H. A. Stone, Diffusiophoresis: from dilute to concentrated electrolytes. *Soft Matter* **16,** 6975-6984 (2020)

[12] H. Ohshima, and K. Furusawa, *Electrical Phenomena at Interfaces: Fundamentals, Measurements, and Applications* (Dekker, New York, 1998) 2nd edn.

[13] C. D. Nadell, K. Drescher, N. S. Wingreen, and B. L. Bassler, Extracellular matrix structure governs invation resistance in bacterial biofilms. *ISME J.* **9**, 1700-1709 (2015)

[14] C. D. Nadell, and B. L. Bassler, A fitness trade-off between local competition and dispersal in *V. cholerae* biofilms. *Proc. Natl. Acad. Sci.* **108**, 14181-14185 (2011)

[15] S. Shim, and H. A. Stone, CO_2-leakage-driven diffusiophoresis causes spontaneous accumulation of charged materials in channel flow. *Proc. Natl. Acad. Sci. U.S.A.* **117**(42) 25985-25990 (2020)

[16] A. Gupta, S. Shim, L. Issah, C. McKenzie, and H. A. Stone, Diffusion of multiple electrolytes cannot be treated independently: Model predictions with experimental validation. *Soft Matter*, **15**, 9965-9973. (2019)

[17] P. Stothard, The sequence manipulation suite: JavaScript programs for analyzing and formatting protein and DNA sequences. *BioTechniques* **28**, 1102-1104 (2000)

[18] L. P. Kozlowski, IPC – Isoelectric point calculator. *Biology Direct* **11**:55 (2016)

[19] Prot pi – Bioinformatics Calculator:
http://www.protpi.ch/Calculator/ProteinTool (2014)

[20] M. Shigematsu, Y. Meno, H. Misumi, and K. Amako, The measurement of swimming velocity of *Vibrio cholerae* and *Pseudomonas aeruginosa* using the video tracking method, *Microbiol. Immunol.* **39**, 741-744 (1995)

[21] S. M. Vater, S. Weiße, S. Maleschlijski, C. Lotz, F. Koschitzki, T. Schwartz, U. Obst, and A. Rosenhahn, Swimming behavior of *Pseudomonas aeruginosa* studied by holographic 3D tracking. *PLoS ONE* **9**(1), e87765 (2014). DOI: https://doi.org/10.1371/journal.pone.0087765

[22] Q. Cai, Z. Li, Q. Ouyang, C. Luo, and V. D. Gordon, Singly flagellated *Pseudomonas aeruginosa* chemotaxes efficiently by unbiased motor regulation. *mBio* **7**(2), e00013-16 (2016). DOI: 10.1128/mBio.00013-16.

[23] S. Kojima, K. Yamamoto, I. Kawagishi, and M. Homma, The polar flagellar motor of *Vibrio cholerae* is driven by an Na^+ motive force. *J. Bacteriol.* **181**, 1927-1930 (1999)

[24] A. Sen, R. K. Nandi, and A. N. Ghosh, Ion-swimming speed variation of *V. cholerae* cells. *J. Biosci.* **30**, 465-467 (2005)

[25] T. Minamino, Y. Imae, F. Oosawa, Y. Kobayashi, and K. Oosawa, Effect of intracellular pH on rotational speed of bacterial flagellar motors. *J. Bacteriol.* **185**, 1190-1194 (2003)